Robust surface-wave full-waveform inversion

Dmitry Borisov[1,2], Fuchun Gao[3], Paul Williamson[3], Frederik J. Simons[1] and Jeroen Tromp[1]*
[1]Princeton University, [2]Kansas Geological Survey, [3]Total EP Research and Technology

SUMMARY

Estimation of subsurface seismic properties is important in civil engineering, oil & gas exploration, and global seismology. We present a method and an application of robust surface-wave inversion in the context of 2D elastic waveform inversion of an active-source onshore dataset acquired on irregular topography. The lowest available frequency is 5 Hz. The recorded seismograms at relatively near offsets are dominated by dispersive surface waves. In exploration seismology, surface waves are generally treated as noise ("ground roll") and removed as part of the data processing. In contrast, here, we invert surface waves to constrain the shallow parts of the shear wavespeed model. To diminish the dependence of surface waves on the initial model, we use a layer-stripping approach combined with an envelope-based misfit function. Surface waves are initially inverted using short offsets (up to 0.6 km) and over a high-frequency range (12.5–15 Hz) to constrain the shallow parts of the model. The lower-frequency components and longer offsets, which can sample deeper parts of the model, are gradually added to the process as the inversion proceeds. At the final stage, surface waves are inverted using offsets of up to 1.5 km over a band between 5–15 Hz. The final V_s model includes high-resolution features in the near surface, and shows good agreement with results from dispersion-curve analysis. The data fit is also greatly improved.

INTRODUCTION

Full-waveform inversion (FWI) (Tarantola, 1984) is a data-fitting approach to estimate properties of the Earth–e.g., compressional (V_p) and/or shear (V_s) wavespeeds–from seismic data, by minimizing the misfit between observed and calculated seismograms. Compared to first-arrival tomography, FWI can provide velocity models at higher resolution without picking and improve the final image in a depth migration workflow (e.g., Plessix et al., 2013). Key factors for a successful inversion typically include an accurate starting model and a targeted acquisition with low-frequency sources and wide angle/aperture surveys (Virieux and Operto, 2009), although this depends on the workflow and the measure of misfit used.

In land seismics, a surface source generates high-amplitude surface waves. Although these are widely used in global and regional seismology (Simons et al., 1999) and shallow engineering (Smith et al., 2018) studies, they are typically treated as noise within the seismic exploration community. In this study, we use surface waves to obtain valuable information on the shallow velocity structure which, if recovered, may reduce the need for statics estimation. Surface waves are commonly inverted using spectral (SASW) (Nazarian and Stokoe, 1984) and multi-station (MASW) (Xia et al., 1999) analyses, which can generate local 1D profiles of V_s by inverting dispersion curves. FWI, on the other hand, produces full volumes of the subsurface properties by inverting entire seismograms.

In this paper, we first recall the gradient expressions for global correlation (GC) norms. We then present a synthetic example based on a field case study. To accurately simulate the wavefield in a model with irregular topography, we use a spectral-element (SEM) solver (Komatitsch and Tromp, 1999). We show that conventional FWI is easily trapped in local minima, while our approach is stable and can converge using an inaccurate starting model. We then present a field example from onshore Argentina. The final V_s model is compared to the results from an inversion of dispersion curves, and the results show good agreement.

METHOD AND WORKFLOW

In this study we perform a time-domain 2D elastic surface-waves full-waveform inversion on land. Because of their dispersive nature, surface waves can be difficult to invert using a conventional l_2 waveform-difference misfit function (Brossier et al., 2009). To address the issue, approaches with alternative misfit functions have been proposed (Solano et al., 2014; Yuan et al., 2015; Borisov et al., 2017). Here we tackle the problem by applying a layer stripping approach (Masoni et al., 2016), where the process starts by inverting surface waves using a narrow offset and a high-frequency range of the data to constrain the shallow parts of the model. We employed a global correlation norm (GC) (Choi and Alkhalifah, 2012), which was shown to be more robust with respect to inaccuracies in amplitudes. For a given model vector $\mathbf{m}$, a global correlation norm $\chi^{\mathrm{GC}}(\mathbf{m})$ is defined as a zero-lag cross-correlation between normalized observed ($\mathbf{d}$) and synthetic ($\mathbf{s}$) traces:

$$\chi^{\mathrm{GC}}(\mathbf{m}) = \sum_r \Big[-\hat{\mathbf{s}}_r(\mathbf{m}) \cdot \hat{\mathbf{d}}_r \Big], \qquad (1)$$

where r is the receiver number. To avoid clutter we omit the explicit dependence of the calculated field on the model $\mathbf{m}$ from here on. We show the expressions only for a single source, so summation over shots should be performed in the multi-source case. The normalized traces are expressed as $\hat{\mathbf{d}}_r = \mathbf{d}_r/||\mathbf{d}_r||$, $\hat{\mathbf{s}}_r = \mathbf{s}_r/||\mathbf{s}_r||$, and "$||\ ||$" indicates the l_2 norm. The corresponding expression for the gradient is:

$$\frac{\partial \chi^{\mathrm{GC}}}{\partial \mathbf{m}} = \sum_r \Big[\frac{\partial \mathbf{s}_r}{\partial \mathbf{m}} \cdot \frac{1}{||\mathbf{s}_r||} \Big\{ \hat{\mathbf{s}}_r(\hat{\mathbf{s}}_r \cdot \hat{\mathbf{d}}_r) - \hat{\mathbf{d}}_r \Big\} \Big]. \qquad (2)$$

The layer-stripping approach results in a frequency continuation which goes in the opposite sense to that normally used in FWI, and so is even more susceptible to cycle-skipping. To deal with this issue at the high frequencies, we employed an envelope-based (Bozdağ et al., 2011) global correlation norm χ^{EGC} (Oh and Alkhalifah, 2018). In equation 1, the observed

10.1190/segam2019-3215047.1

and synthetic traces are replaced by the corresponding envelopes $\mathbf{e}_r^{\mathrm{d}}$ and $\mathbf{e}_r^{\mathrm{s}}$, respectively:

$$\chi^{\mathrm{EGC}} = \sum_r \left[-\hat{\mathbf{e}}_r^{\mathrm{s}} \cdot \hat{\mathbf{e}}_r^{\mathrm{d}} \right]. \quad (3)$$

The corresponding gradient is expressed as:

$$\frac{\partial \chi^{\mathrm{EGC}}}{\partial \mathbf{m}} = \sum_r \left[\frac{\partial \mathbf{s}_r}{\partial \mathbf{m}} \cdot \frac{1}{||\mathbf{e}_r^{\mathrm{s}}||} \left\{ \hat{\mathbf{e}}_r^{\mathrm{s}} \left(\hat{\mathbf{e}}_r^{\mathrm{s}} \cdot \hat{\mathbf{e}}_r^{\mathrm{d}} \right) - \hat{\mathbf{e}}_r^{\mathrm{d}} \right\} \right]. \quad (4)$$

Once convergence is achieved, we switch to χ^{GC}. At this stage, more details should be produced by the inversion update. The lower-frequency components and longer offsets, which sample deeper part of the model, are gradually added as the inversion proceeds to update the deeper parts.

We also update the input source wavelet during the inversion process in the manner of Pratt (1999). Such an approach can significantly improve the inversion effectiveness on field data, where an accurate estimate of the source-time function is not available, and the physics of wave propagation is not properly taken into account (Groos et al., 2014). Since surface waves have a limited sensitivity to V_p and density parameters, only V_s is inverted. The inversion is carried out using the Python-based open-source package SeisFlows (Modrak et al., 2018), which uses external software, such as SPECFEM2D (Komatitsch and Tromp, 1999), to perform forward simulations. In our examples, we use the L-BFGS quasi-Newton method to calculate search directions. A step length is computed using a line search algorithm.

SYNTHETIC EXPERIMENTS

For the synthetic experiments we generate a model based on a field study described in the next section. The model is about 15 km×1.7 km in the horizontal (x) and vertical (z) directions, respectively (Figure 1). Note that we cut the edges and show only the top most 0.4 km since the majority of SWI updates occur within this area. The initial V_p model was derived from first-break traveltime tomography. The initial V_s model (Figure 1b) was derived from the initial V_p model using a ratio of $V_p/V_s = 1.7$, and the density model was obtained by using Gardner relationship. The topmost part of the target V_s model contains a low-velocity layer (LVL) about 75 m thick (Figure 1a), which is based on MASW results from the field experiment. The target models of $\{V_p, V_s, \rho\}$ also have four rectangular inclusions of different dimensions and various perturbations. The mesh was generated using 15,708 elements, on average 40 m×40 m each. Since five GLL integration points per element side are used in our implementation, the actual wavefield discretization, on average, is equal to about 10 m, and the exact total number of grid points in the mesh equals 252,993. There are two canyons crossing the line at $x = 6$ km and $x = 9.2$ km, with overall topographic variations of about 50 m. We used 144 vertical-force sources and 601 vertical-component receivers regularly distributed on the surface between $x = 1.48$ km and 13.48 km. Each source is represented by a Ricker wavelet with a dominant frequency of 40 Hz. To

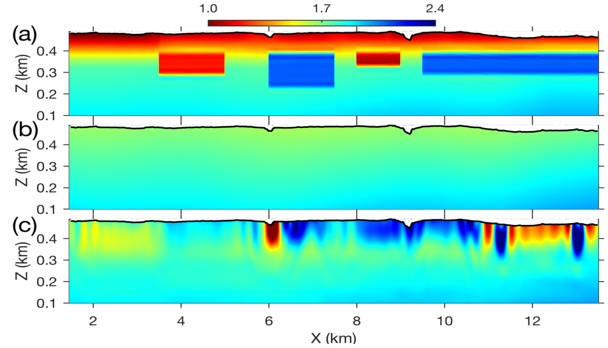

Figure 1: V_s models from the synthetic SWI: (a) target, (b) initial, and (c) final SWI models. Note that SWI did not converge due to cycle skipping.

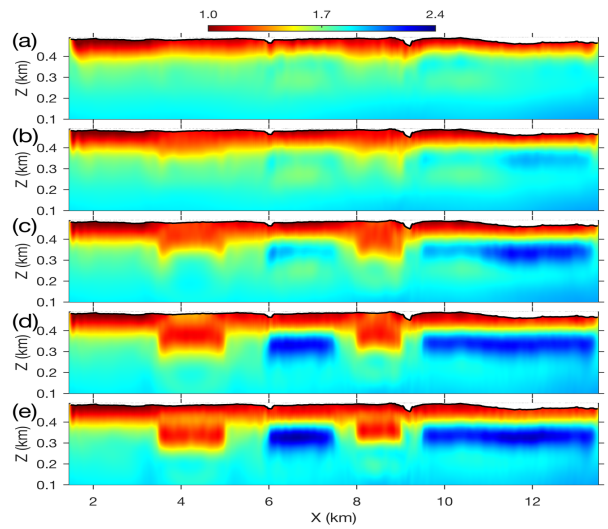

Figure 2: V_s models from the synthetic SWI. The results at five frequency scales are shown: (a) 12.5–15 Hz, (b) 10–12.5 Hz, (c) 7.5–10 Hz, (d) 5–7.5 Hz, and (e) 5–15 Hz. Note the gradual update of the deeper parts.

make the tests more realistic, we apply a low-cut filter below 5 Hz.

In the first test, we immediately start with χ^{GC} to invert narrow offset (up to 0.6 km) and high- frequency (12.5–15 Hz) data to constrain the shallow part of the model. Because the initial model is not accurate enough, cycle skipping occurs and the inversion is not able to converge (Figure 1c). To tackle this issue, in the second experiment we employed an envelope-based misfit function χ^{EGC}, which improves the topmost part (Figure 2a). We then sequentially use 10–12.5 Hz, 7.5–10 Hz, and 5–7.5 Hz frequency bands and limit the offsets to 0.8 km, 1.0 km, and 1.5 km, respectively. Lower-frequency and longer-offset data sample the deeper parts and gradually improve the model (Figures 2b-d). At the final stage, surface waves are inverted using an offset up to 1.5 km range over the band 5–15 Hz (Figure 2e). The vertical V_s profiles at $x = 4$ km and $x = 10$ km show that the inversion accurately retrieves the LVL in the near-surface,

10.1190/segam2019-3215047.1

and all rectangular inclusions (Figure 3). The data fit is greatly improved (Figure 4) with the final synthetics almost indistinguishable from the observations (Figure 4e,f). We also performed an elastic SWI of anelastic data with $Q = 50$ (Figure 5). Although the results are not bad, it indicates that for higher Q values, special care of attenuation should be taken.

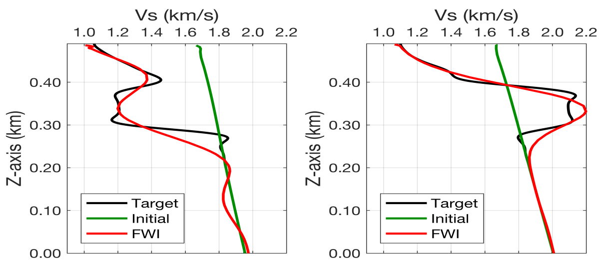

Figure 3: Vertical profiles of V_s results from synthetic SWI at $x = 4$ km (left) and $x = 10$ km (right).

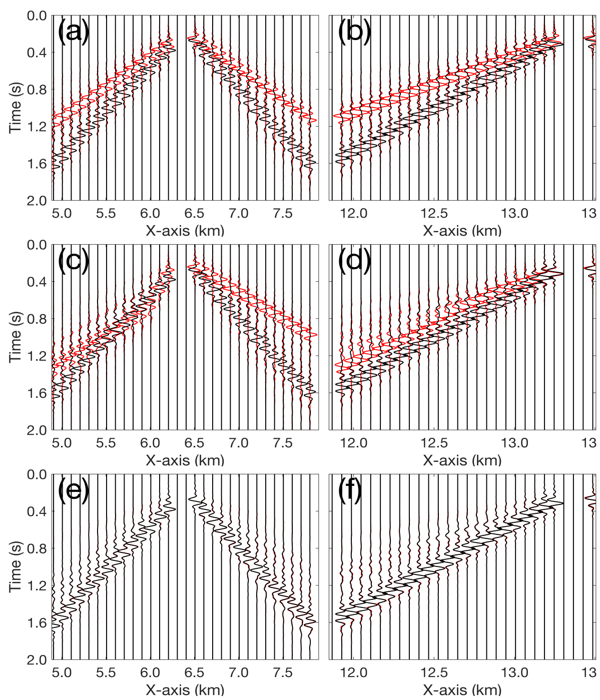

Figure 4: Synthetic data comparison. Observations (black) and synthetics (red), band-passed between 5 and 15 Hz for a source located at $x = 6.4$ km (left) and $x = 13.5$ km (right). Data fit from: (a–b) initial model (Figure 1b), (c–d) SWI model with χ^{GC} alone, (e-f) SWI model with χ^{EGC} and χ^{GC} combined.

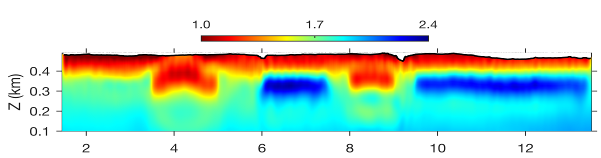

Figure 5: V_s models from the synthetic SWI with $Q = 50$.

FIELD EXAMPLE

The field example consists of a 12-km long 2D line from onshore Argentina. The line is located on the bottom of a mountainside. Several superimposed alluvial fans originating from the top of the mountain have deposited layers of debris on top of sedimentary bedrock, creating a low-velocity near-surface layer (Masoni, 2016). We use the same initial V_s model as in the synthetic test, but we only plot the upper 120 m and use a different color scale (Figure 6) for a better comparison with inversion results. In total, 600 shot gathers were recorded using 20 m spaced Vibroseis sources, with the sweep signal starting from about 4.5 Hz. We use a subset of 144 sources and all 601 receiver groups. The main steps of data pre-processing include polarity correction for certain traces, amplitude correction for 3D geometrical spreading, removal of instrument response and velocity-to-displacement conversion.

We sequentially apply the same parameters (e.g., frequency bands and maximum offsets) as in the synthetic example. The inverted V_s models at each stage are shown in Figure 7. The final V_s model (Figure 7e) is compared with the result from the dispersion-curve analysis provided by a contractor (Figure 8). Although there is much more lateral variation in the final SWI model, there is a good structural agreement between the results obtained from the two different methods. For instance, SWI retrieves the near-surface LVL by reducing the initial V_s values by more than 0.5 km/s in most shallow locations. To compare the data fit, we plot observed and synthetic seismograms calculated in the initial and final models for one source located at $x = 6.4$ km. Overall, a trace-by-trace comparison of the waveforms band-passed between 5 and 15 Hz illustrates significant improvement in data fitting.

CONCLUSIONS

We developed a method to make surface wave inversion robust in the framework of elastic waveform inversion, and applied it to a land dataset acquired on a moderately irregular topography to update the shallow parts of a V_s model. The method can provides results comparable on the macro-scale to dispersion-curve analysis with poor initial models, but without the 1D assumption of the latter. It was also shown to be robust with respect to attenuation, lateral and topography variations. The inversion results may lead to a better understanding of shallow substructures with direct implications for geophysical engineering and for improved imaging of deeper targets in exploration studies.

ACKNOWLEDGMENTS

We thank Total E&P Research and Technology for providing financial support and computational resources. In particular, we thank Bertrand Duquet, Isabella Masoni, and Jean-Luc Boelle for fruitful discussions. Special thanks go to Total Austral for permission to publish this work and data provision during the project.

10.1190/segam2019-3215047.1

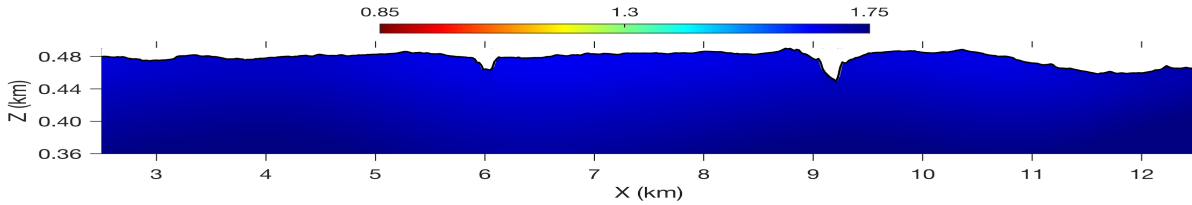

Figure 6: Zoom of the topmost part of the V_s initial model.

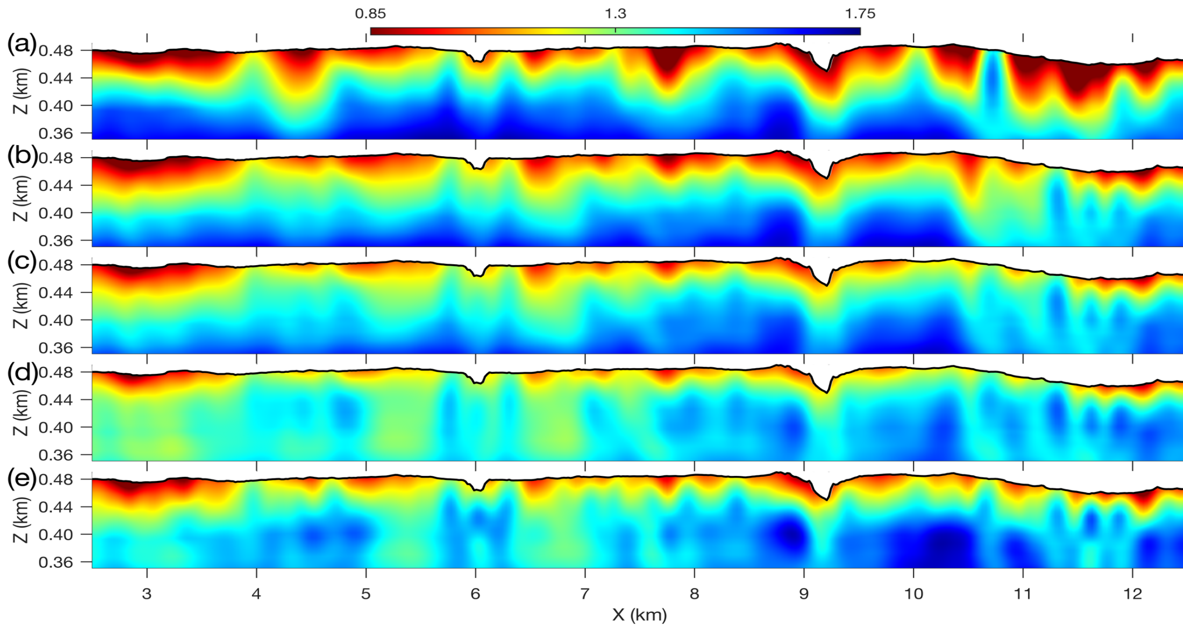

Figure 7: Zoom of the shallow part of the inverted V_s models at different scales: (a) 12.5–15 Hz, 0.6 km offset; (b) 10–12.5 Hz, 0.8 km offset; (d) 7.5–10 Hz, 1 km offset; (d) 5–7.5 Hz, 1.5 km offset; (e) 5–15 Hz, 1.5 km offset.

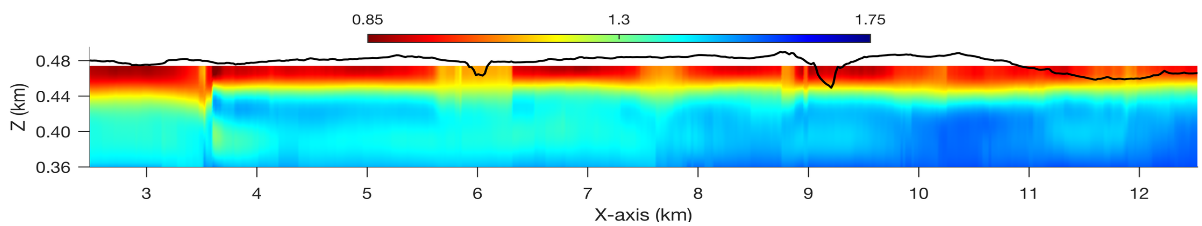

Figure 8: V_s model obtained from analysis of dispersion curves.

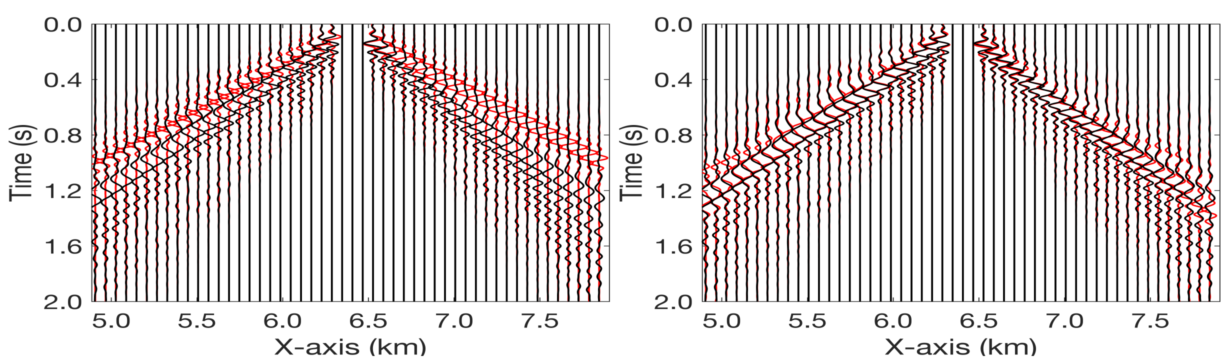

Figure 9: Field data comparison. Observations (black) and synthetics (red), band-passed between 5 and 15 Hz for a source located at $x = 6.4$ km. Left and right panels correspond to traces before and after SWI, respectively.

10.1190/segam2019-3215047.1

REFERENCES

Borisov, D., R., Modrak, F., Gao, and J., Tromp, 2017, 3D elastic full-waveform inversion of surface waves in the presence of irregular topography using an envelope-based misfit function: Geophysics, **83**, no. 1, R1–R11, doi: https://doi.org/10.1190/geo2017-0081.1.

Bozdag, E., J., Trampert, and J., Tromp, 2011, Misfit functions for full waveform inversion based on instantaneous phase and envelope measurements: Geophysical Journal International, **185**, 845–870, doi: https://doi.org/10.1111/j.1365-246x.2011.04970.x.

Brossier, R., S., Operto, and J., Virieux, 2009, Seismic imaging of complex onshore structures by 2D elastic frequency- domain full-waveform inversion: Geophysics, **74**, no. 6, WCC105–WCC118.

Choi, Y., and T., Alkhalifah, 2012, Application of multi-source waveform inversion to marine streamer data using the global correlation norm: Geophysical Prospecting, **60**, 748–758, doi: https://doi.org/10.1111/j.1365-2478.2012.01079.x.

Groos, L., M., Schafer, T., Forbriger, and T., Bohlen, 2014, The role of attenuation in 2D full-waveform inversion of shallow-seismic body and Rayleigh waves: Geophysics, **79**, no. 6, R247–R261, doi: https://doi.org/10.1190/geo2013-0462.1.

Komatitsch, D., and J., Tromp, 1999, Introduction to the spectral element method for three-dimensional seismic wave propagation: Geophysical Journal International, **139**, 806–822, doi: https://doi.org/10.1046/j.1365-246x.1999.00967.x.

Masoni, I., 2016, Inversion of surface waves in an oil & gas exploration context: Ph.D. thesis, Université de Grenoble.

Masoni, I., J.-L., Boelle, R., Brossier, and J., Virieux, 2016, Layer stripping FWI for surface waves: 86th Annual International Meeting, SEG, Expanded Abstracts, doi: https://doi.org/10.1190/segam2016-13859781.1.

Modrak, R., D., Borisov, M., Lefebvre, and J., Tromp, 2018, The SeisFlows framework for waveform inversion: rapid prototyping and HPC applications: Computers and Geosciences, **115**, 88–95, doi: https://doi.org/10.1016/j.cageo.2018.02.004.

Nazarian, S., and K., Stokoe, 1984, In situ shear wave velocities from spectral analysis of surface waves: 8th Conference on Earthquake Engineering, 3, 31–38.

Oh, J.-W., and T., Alkhalifah, 2018, Full waveform inversion using envelope-based global correlation norm: Geophysical Journal International, **213**, 815–823, doi: https://doi.org/10.1093/https://doi.org/gjihttps://doi.org//ggy031.

Plessix, R., P., Milcik, H., Rynja, A., Stopin, K., Matson, and S., Abri, 2013, Multiparameter full-waveform inversion: Marine and land examples: The Leading Edge, **32**, 1030–1038, doi: https://doi.org/10.1190/tle32091030.1.

Pratt, R. G., 1999, Seismic waveform inversion in the frequency domain, part 1: Theory and verification in a physical scale model: Geophysics, **64**, 888–901, doi: https://doi.org/10.1190/1.1444597.

Simons, F. J., A., Zielhuis, and R. D., Van Der Hilst, 1999, The deep structure of the Australian continent from surface wave tomography: Lithos, **48**, 17–43, doi: https://doi.org/10.1016/S0024-4937(99)00041-9.

Smith, J., D., Borisov, R., Modrak, and J., Tromp, 2018, A practical approach to seismic imaging of tunnels using 3D full-waveform inversion: Geophysics, **83**, 1–53.

Solano, C. P., D., Donno, and H., Chauris, 2014, Alternative waveform inversion for surface wave analysis in 2-D media: Geophysical Journal International, **198**, 1359–1372, doi: https://doi.org/10.1093/https://doi.org/gjihttps://doi.org//ggu211.

Tarantola, A., 1984, Inversion of seismic reflection data in the acoustic approximation: Geophysics, **49**, 1259–1266, doi: https://doi.org/10.1190/1.1441754.

Virieux, J., and S., Operto, 2009, An overview of full-waveform inversion in exploration geophysics: Geophysics, **74**, no. 6, WCC1–WCC26.

Xia, J., R. D., Miller, and C. B., Park, 1999, Estimation of near-surface shear-wave velocity by inversion of Rayleigh waves: Geophysics, **64**, 691–700, doi: https://doi.org/10.1190/1.1444578.

Yuan, Y. O., F. J., Simons, and E., Bozdag, 2015, Multiscale adjoint waveform tomography for surface and body waves: Geophysics, **80**, no. 5, R281–R302, doi: https://doi.org/10.1190/geo2014-0461.1.